ChemElectroChem

Research Article
doi.org/10.1002/celc.202101537

Chemistry Europe
European Chemical Societies Publishing

www.chemelectrochem.org

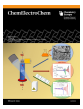

Insight into the Cycling Behaviour of Metal Anodes, Enabled by X-ray Tomography and Mathematical Modelling

Francesca Rossi,[b] Lucia Mancini,[c] Ivonne Sgura,[d] Marco Boniardi,[e] Andrea Casaroli,[e] Alexander Peter Kao,[c] and Benedetto Bozzini*[a]

This work tackles the methodological challenge of rationalizing symmetric-cell cycling data from a materials-science perspective, through experiment replication, mathematical modelling, and tomographic imaging. Specifically, we address Zn electrode cycling in alkaline electrolyte with and without adding tetrabutylammonium bromide (TBAB). This additive is known from literature, but its practical impact is jeopardized by lack of in-depth understanding of its behaviour. Electrochemical testing was carried out at practically relevant current densities and the effect of variations of operating conditions was taken into account. The physical chemistry underlying cell potential profiles, has been modelled mathematically, accounting for: electrokinetics, mass-transport, electrode shape change and passivation. In particular, we disclosed an unexpected joint effect of TBAB and current density on passivation time: tomography allowed to rationalise this behaviour in terms of precipitate morphology.

Introduction

Rechargeable Li and post-Li batteries with metal anodes, are among the most promising technologies to develop high energy- and power-density devices.[1–4] Notwithstanding the appeal of these electrodes, their practical use is delayed by poorly understood and hardly controllable shape changes, that lead to capacity fade and short circuits.

In response to this situation, a deluge of papers is appearing in the literature, often conveying empirical experimental information that is poorly substantiated from the statistical, instrumental and theoretical viewpoints. Moreover, theoretical tools are seldom used in a quantitative and systematic way to rationalize vast corpora of measured data. In the present context, both the quality of experiments and the valuing of data call for improvement with respect to the state-of-the-art.

In this scenario, the present manuscript contributes jointly to three challenges: (i) the achievement of novel experimental information, combining electrochemistry and 3D X-ray imaging; (ii) the proposal of a solid methodology for the generation of reliable and quantitative datasets, that can be employed for data-driven materials-science advancement; (iii) the proposal of a novel, physico-chemically transparent, mathematical model and its practical use for the rationalization of experimental datasets. Our model enables extraction of quantitative information from cycling time-series regarding: electrocrystallization, passivation, mass-transport and electrokinetics. Parameter decoupling analysis and data assimilation allow for effective and reliable theory-based rationalization of large datasets.

From the materials perspective, this paper addresses the cycling behaviour of metallic Zn anodes in alkaline electrolytes without and with added tetrabutyl-ammonium bromide (TBAB). Despite their environmental and economic appeal, rechargeable Zn-based devices are still far from commercialization, primarily owing to the low cyclability of the anode. Specifically, it is well-known that the performance of the Zn anode in traditional alkaline electrolytes, is affected by three major problems: (i) passivation during the discharge process, owing to the precipitation of ZnO from zincate solutions; (ii) self-discharge due to hydrogen evolution, and (iii) shape changes, specifically dendrite growth, during the charge process.[5–8] All these disadvantages can be attenuated by use of additives. Organic surfactants are considered as promising candidates, thanks to their low cost and toxicity: their specific action is related to the ability to adsorb onto the electrode surface, promoting lateral growth and limiting the deposition of the passivating species.[9–11] Notwithstanding the presence of a considerable number of publications on organic additives, a rational and quantitative description of the mechanisms underlying their beneficial action is still lacking. In a previous work of

[a] Prof. Dr. B. Bozzini
Department of Energy
Politecnico di Milano
via Lambruschini 4, 20156 Milano, Italy
E-mail: benedetto.bozzini@polimi.it
[b] Dr. F. Rossi
Department of Innovation Engineering
University of Salento
via Monteroni, 73100 Lecce, Italy
[c] Dr. L. Mancini, Dr. A. P. Kao
Elettra – Sincrotrone Trieste S.C.p.A.
S.S. 14-km 163.5 in Area Science Park, 34149 Basovizza, Trieste, Italy
[d] Prof. Dr. I. Sgura
Department of Mathematics and Physics
University of Salento
via per Arnesano, 73100 Lecce, Italy
[e] Prof. M. Boniardi, Dr. A. Casaroli
Department of Mechanics
Politecnico di Milano
via la Masa 1, 20156 Milano, Italy

Supporting information for this article is available on the WWW under https://doi.org/10.1002/celc.202101537

ours,[12] we performed a systematic and quantitative electrochemical investigation on the impact of quaternary ammonium salts (QAS) and ionomers (QAI) on Zn electrodeposition and passivation processes. We demonstrated that, during Zn cycling, organic molecules with QA moieties tend to influence jointly both the cathodic and anodic processes, tending to suppress the accumulation of anodic byproducts and promoting symmetric cathodic and anodic activation. We pinpointed that TBAB is a particularly promising additive, and similar conclusions had been drawn also in,[13–15] on the basis of empirical considerations.

The materials-science case addressed in the present paper, is thus a deepening of the study of the behaviour of TBAB in alkaline electrolytes, based, on the one hand, on galvanostatic cycling of Zn electrodes in symmetrical Zn/Zn split cells of 2032 coin-cell geometry, and, on the other hand, on imaging and mathematical modelling. Exhaustive literature analysis identified a close-knit group of publications on alkaline symmetrical Zn cells,[16–20] employing galvanostatic cycling in the current-density range $0.25 \div 10\ mA\,cm^{-2}$: only in[18] additives were considered. It is worth noting that it is very rare to find mention of experiment replication or estimation of experimental uncertainties. The state-of-the-art in the field of symmetrical cell testing with Zn electrodes in alkaline ambient is that, qualitatively, all publications agree on the conclusion that the passivation of the anode is the principal process affecting the cyclability, with the exception of[20] in which short-circuiting is reported. Specifically,[17,19] recorded the same cell lifespan (10 hours) at different applied cell capacities (0.3 and $1\ mAh\,cm^{-2}$, respectively), while Yu *et al.*[20] observed different cell lifespan values, ranging from 21 to 250 hours, depending on the cell capacity employed. A different scenario is presented in,[18] where the cell is run for 250 hours in the presence of different surfactants and the variations on the voltage profiles were monitored, though without drawing physico-chemical indications from their differences.

In the present multi-technique work, electrochemical measurements are complemented by imaging, based on: (i) *post mortem* SEM – yielding information on the morphology of disassembled electrodes –, and (ii) X-ray computed microtomography (μ-CT) – allowing to characterize in 3D the morphological features of the intact assembled cell.

Results and Discussion

Symmetrical cells are a powerful tool for the study of the rechargeable battery electrodes, since they allow to decouple anodic and cathodic effects. In accordance with observations by Glatz *et al.*,[21] we performed galvanostatic charge-discharge (GCD) cycles at two current densities: 1 and $10\ mA\,cm^{-2}$, with associated capacities of 0.5 and $5\ mA\,h\,cm^{-2}$, respectively. The GCD cycles, illustrated in Section 4, were run with a cut-off of ± 1 V, corresponding to cell failure by passivation. All our measurements were replicated an appropriate number of times, as detailed below, to gain insight into the degree of the reproducibility of these systems. Particular experimental and theoretical attention was paid to the shape of the transients constituting the voltage profiles, because they are strongly diagnostic of the electrokinetic, mass-transport and electrocrystallization processes that control the behaviour of the electrodes during cell operation. In this research, we studied systematically additive-free and TBAB-containing electrolytes, immobilized in a glass-fibre separator, at 1 (Figure 1) and $10\ mA\,cm^{-2}$ (Figure 3): these results are discussed in Sections 2.1–2.4. These data have been complemented (see details in the Supporting Information) by the investigation of the effect of: (i) other current densities (Figures S1-A and S1-B); (ii) different electrolyte volumes (Figure S1-D); (iii) different depth of discharge (Figure S1-E) and (iv) use of free electrolyte (Figure S1-F). Moreover, in Section 2.5 we have carried out an analysis of all the measured chronopotentiometric time-series, based on the mathematical properties of the model detailed in Section S3 of the Supporting Information, aimed at extracting physico-chemical information from the experimental data. Specifically, we addressed the following key aspects: (i) a classification of the overvoltage dynamics observed in the single galvanostatic half-periods (Figure 4); (ii) the metal outgrowth rates (Table 1) and (iii) the passivation rates (Table 2). Full details on numerical analysis and computations are also provided in Section S3 of the Supporting Information.

Additive-free electrolyte: 1 $mA\,cm^{-2}$

In Figure 1-A we show three replicated experiments at $1\ mA\,cm^{-2}$ with the additive-free electrolyte. The cell behaves in a reasonably reproducible way, before reaching the passivation

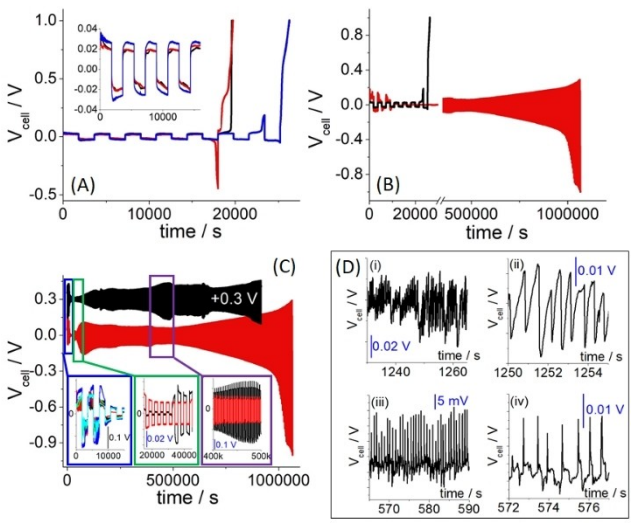

Figure 1. Voltage profiles from replicated galvanostatic charge-discharge cycling of Zn/Zn symmetrical cells (6 M KOH + 0.1 M ZnO, glass fibre separator) at $1\ mA\,cm^{-2}$. (A) No additive. Inset: magnification of the first 16,000 s. (B) Measurements without (black) and with 0.3 mM TBAB (red). (C) Two replicated runs with 0.3 mM TBAB, with magnification of representative portions of the voltage profiles. (D) Representative data-chunks (i, iii) and some of their details (ii, iv), showing relaxation potential oscillations developing in the initial period of galvanostatic polarization with 0.3 mM TBAB.

Table 1. Outgrowth time constants τ_{out} (black numbers) and corresponding model F_C parameter values (red numbers) from analysis of galvanostatic cycling chronopotentiometric series. The figures containing the data, from which the time constants have been evaluated, are indicated in blue.

experim. condition	0.25 mA cm^{-2} no addit. τ_{out} (s) F_C	1 mA cm^{-2} no addit. τ_{out} (s) F_C	5 mA cm^{-2} no addit. τ_{out} (s) F_C	10 mA cm^{-2} no addit. τ_{out} (s) F_C	1 mA cm^{-2} TBAB τ_{out} (s) F_C	10 mA cm^{-2} TBAB τ_{out} (s) F_C
separator	531 ± 91 18.0 ± 3.3 Fig. S1A	544 ± 60 17.5 ± 2.1 Fig. 1A	73 45.6 Fig. S1F	21.0 ± 2.6 50.6 ± 0.3 Fig. 3A	1120 ± 200 5.45 ± 2.27 Fig. 1B,C	2010 ± 150 0.897 ± 0.277 Fig. 3B, C)
free electrolyte		526 ± 34 18.2 ± 1.3 Fig. S1E				

Table 2. Passivation time t_{pass} (black numbers) and corresponding model parameter k_{pass} (red numbers) from analysis of galvanostatic cycling chronopotentiometric series. The figures containing the data, from which the time constants have been evaluated, are indicated in blue. [+]Experiments with different electrolyte volumes. [†]Experiments with different depths of discharge.

Experim. condition	0.25 mA cm^{-2} no addit. t_{pass} (ks) k_{pass} ($\times 10^5$)	1 mA cm^{-2} no addit. t_{pass} (ks) k_{pass} ($\times 10^5$)	5 mA cm^{-2} no addit. t_{pass} (ks) k_{pass} ($\times 10^5$)	10 mA cm^{-2} no addit. t_{pass} (ks) k_{pass} ($\times 10^5$)	1 mA cm^{-2} TBAB t_{pass} (ks) k_{pass} ($\times 10^5$)	10 mA cm^{-2} TBAB t_{pass} (ks) k_{pass} ($\times 10^5$)
separator	22.5 ± 2.5 12.2 ± 2.0 Fig. S1A	21.9 ± 3.8 12.7 ± 3.4 Fig. 1A, S1D[+], S1E[†]	42.1 4.89 Fig. S1B	77.6 ± 3.8 2.00 ± 0.14 Fig. 3A	923 ± 10 (5.34 ± 0.09) $\times 10^{-2}$ Fig. 1B,C	29.7 ± 10.0 8.15 ± 4.77 Fig. 3B, C
free electrolyte		38.0 ± 10.5 5.68 ± 2.57 Fig. S1F				

cut-off with a limited spread of failure times. In particular, as highlighted in the inset of Figure 1-A and discussed more extensively below in Section 2.5, the shape of the voltage profiles is quite consistent and can be explained in terms of straightforward cathodic and anodic metal electrochemistry. The half-cycles showing a rapidly increasing initial portion, followed by a maximum, after which the voltage decreases, correspond to nucleation followed by outgrowth of Zn. Instead, half-cycles exhibiting a continuous overvoltage increase denote gradual passivation. Cases in which the cell potential decreases without being preceded by a maximum, indicate low nucleation overvoltage. In the absence of additives (Figure 1-A), the first few cycles are dominated by cathodic nucleation and growth, while passivation takes over control at later stages, eventually leading to cell failure in ca. 6 ± 1 hours (see Table 2).

Post mortem X-ray μ-CT Figure 2-A (see also Figure S6-A) shows extensive granularity at the electrode surface, accompanied by the formation of Zn-containing particles in the electrolyte region. The former process is due to the alternation of cathodic metal outgrowth, leading to dead metal, followed by its passivation and by precipitation of ZnO. Syncrotron-Radiation (SR) μ-CT (Figure 2-E) allows to better visualize the extended electrode/electrolyte interface: grain dimensions are micrometric close to the compact metal layer, and extend to several tens of microns, moving into the electrolyte region.

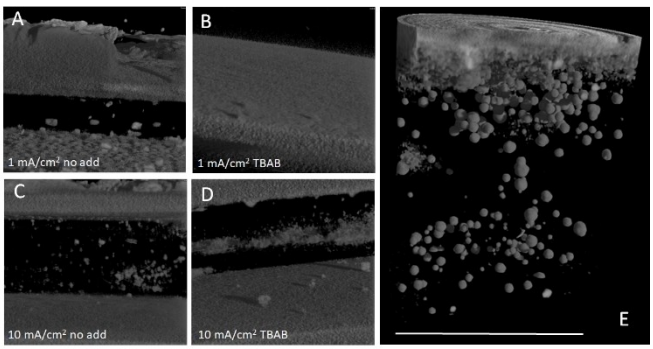

Figure 2. *Post mortem* volume renderings of intact cells (diameter 18 mm), operated at the indicated current densities with additive-free and TBAB-containing electrolytes. Images were obtained by (A–D) microfocus X-ray computed tomography (μ-CT), and (E) synchrotron radiation computed microtomography. Image (E) is from the same region as (A): detail measured in a region located 3 mm from the edge. The scale-bar corresponds to 1 mm.

Electrolyte with addition of TBAB: 1 mA cm^{-2}

Experiments carried out with the addition of TBAB, show a dramatically changed scenario, as depicted in Figure 1-B: (i) the cell lifespan increases by a factor of ca. 40 (see Table 2) and (ii) oscillatory behaviour of the voltage is found during the first few cycles. In order to assess the reproducibility of the potential response, we replicated the full experiment (Figure 1-C) and we repeated the measurement four more times in the initial period of ca. 4 hours (inset of Figure 1-C and Table 2). Moreover, to better highlight the potential oscillations, we carried out a

galvanostatic test without current switching for 3 hours (Figure 1-D). The two long-term replicated experiments reported in Figure 1-C, one of which was stopped after ca. one week of cycling and the other was continued until cell failure, show a remarkable reproducibility of the complex cell dynamics. In a first interval, oscillatory behaviour dominates. Subsequently, a sharp decrease of the cell voltage occurs (see Table 1), reaching a condition in which ohmic control dominates (ca. 20,000 ÷ 35,000 s), owing to the formation of labile short circuit conditions, resulting from contact of dead metal particles. This interval is terminated by a slight increase of overvoltage, related to the formation of dead Zn, characterized by asymmetric nucleation/growth (upper electrode) and passivation (lower electrode) contributions. In prolonged cycling measurements, cell potential asymmetries develop: (see also Figures 1-A (inset), 3-A, 3-C, S1-A and S1-F), due to hydroxide precipitation, preferentially passivating the bottom electrode. This last effect has been explicitly modelled and are detailed in Section S3 of the Supporting Information. The long-term behaviour, characterized by a small modulation of the voltage envelope, stabilizes for several days (Figure 1-C and Table 2) until final passivation (black plot of Figure 1-C). A similar modulated behaviour of the cell voltage profile has also been reported in.[18]

As noted above, the cell-voltage time series measured during the first few cycles (Figures 1-C and 1-D), show an oscillating behaviour, superimposed to a decreasing overvoltage trend, corresponding to electrode area increase. This complex, but consistent scenario is compatible with the observation of both cathodic[21–23] and anodic[24–27] oscillating behaviour of Zn in alkaline electrolytes. These phenomena have been explained with cathodic[28] and anodic[29,30] pseudo-passivation, leading to the precipitation and failure of interfacial films, triggering relaxation oscillations.[31] We have recently rationalized this type of oscillating behaviour on the basis of the DIB (from the names of the authors: Deborah, Ivonne, Benedetto) model of electrochemical phase formation :[32] relaxation oscillations have been shown to originate from a balance of the rate of adsorption at the cathode of an additive and its inhibiting effect on electrodeposition. *Post mortem* μ-XCT Figure 2-B (see also Figure S6-B) highlights that TBAB leads to a much smoother electrode/electrolyte interface, with just a few isolated outgrowth features. Moreover, no precipitation of Zn-containing particles can be observed.

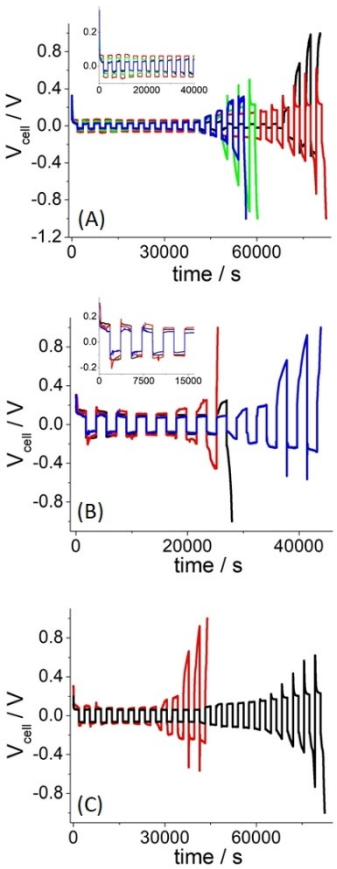

Figure 3. Voltage profiles from replicated galvanostatic charge-discharge cycling of Zn/Zn symmetrical cells (6 M KOH + 0.1 M ZnO, glass fibre separator) at 10 mA cm^{-2}. (A) No additive. Inset: magnification of the first 40,000 s. (B) Replicated runs with 0.3 mM TBAB. Inset: magnification of the first 16,000 s. (C) Comparison cell voltage profiles measured without (black) and with 0.3 mM TBAB (red).

Additive-free electrolyte: 10 mA cm^{-2}

Four replicated experiments at 10 mA cm^{-2} with the additive-free alkaline electrolyte, are shown in Figure 3-A. Also in this case, the repeated time series are remarkably reproducible during the interval of stable cell operation (see inset). The shape of the voltage profiles is quite different with respect to those observed at 1 mA cm^{-2}: nucleation and growth dominate before the inception of passivation processes after ca. 40,000 s of cycling. Cell failure takes place after 19 ± 4 hours of operation (Table 2). It is worth noting that passivation occurs after notably longer operation at 10 than at 1 mA cm^{-2}. This observation, that is in keeping with the results of work on near-neutral Zn symmetrical cells with 3 M $ZnSO_4$,[21] is in part counterintuitive. In fact, one is led to anticipate that electrodeposition at higher rate would bring forward failure. Instead, the stabilization of depassivation takes over control of the cycling behaviour.

Indeed, at higher current densities, the metal oxidation rate is not limited in voltage by the formation of type-II $Zn_{x+1}O$, and it largely overcomes the precipitation rate of type-I ZnO.[33] *Post mortem* X-ray μ-CT Figure 2-C (see also Figure S6-C) reveals a notably smoother surface morphology, with respect to that generated by cycling at 1 mA cm^{-2}, accompanied by a considerable amount of bulk precipitates in the electrolyte, coherently with the electrochemical response.

Electrolyte with addition of TBAB: 10 mA cm^{-2}

While TBAB increases cell lifetime at 1 mA cm^{-2}, at 10 mA cm^{-2} this additive notably decreases it (Figures 3-B, 3-C and Table 2), bringing it down to 9 ± 3 hours. The oscillating behaviour found in the presence of TBAB at 1 mA cm^{-2}, is confirmed also at

10 mA cm^{-2} and the same explanation applies. As far as the shape of the voltage profiles is concerned, the additive moves up the overvoltage increase, characteristic of passivation. *Post mortem* X-ray μ-CT Figures 2-D and S6-D indicate that the tendency to bulk precipitation of ZnO is favoured by TBAB at 10 mA cm^{-2}, showing preferential precipitate formation in correspondence of the planes of contact between separator discs, where a higher proportion of free electrolyte forms. This type of bulk precipitation is probably a result of the interaction between the QAS and zincates, such as pectization, controlling the precipitation of type-I ZnO. In addition, 3D imaging shows that addition of TBAB at 10 mA cm^{-2}, correlates with electrodic outgrowth features, which were not present in the additive-free system (compare Figures 2-C and 2-D also see also Figures S6-C and S6-D). This dependence of additive effect on current density is an aspect poorly addressed in the literature, but of notable practical momentum, and it warrants deepening. In particular, two directions ought to be investigated: on the one hand, better insight is required into the interaction of additives with anodic products and on the other hand, explicit kinetic modelling of the levelling effects is needed. Regarding the latter factor, a first approach to rationalization is possible using literature electrodeposition theories, such as the partial current-density model of levelling (see, e.g.,[34] Chapt 3.8 and references therein) and the DIB model of shape change during electrodeposition (see, e.g.,[35] specifically regarding the effect on morphology evolution of growth inhibition by adsorbed electroactive species).

As detailed in Section 4, we performed additional tests, to understand the sensitivity of the cell performance to changes in operating conditions: these complementary results – that confirm the scenario presented above in this Section – are reported in the Supporting Information.

Analysis of the chronopotentiometric time-series measured during symmetric-cell cycling

This Section describes the analysis of the whole set of the chronopotentiometric time-series measured in all different experimental conditions considered in this study. Systematic literature review reveals the importance of carrying out comprehensive analyses of cycling data, because the rich information contained in experimental time-series is seldom exploited, since attention is mainly paid to the simple assessment of the time to cell failure.

In this work, we propose a model, detailed in Section S3 of the Supporting Information, that enables to follow the potential transients resulting from the application of a galvanostatic square wave, with a PDE system coupling the material balance for the electroactive metal species and the potential of the electrolyte phase. The irreversibilities, caused by metal outgrowth and passivation, are described through the boundary conditions. A small set of physically transparent model parameters allows to capture the variety of transients observed in this study: (i) the effective diffusion coefficient D, accounting for changes in electrolyte chemistry; (ii) the number density of nuclei N_{nucl} forming during the cathodic interval; (iii) the outgrowth rate F_C and (iv) the passivation rate k_{pass}.

Figure 4-A summarizes the chronopotentiometric transient types observed during the galvanostatic half-periods, expounded in Sections 2.1–2.4, classified according to the approach of Section S3 of the Supporting Information. In the experiments without additive, upon progressive increase of the current density, the transient shape changes: (i) from a

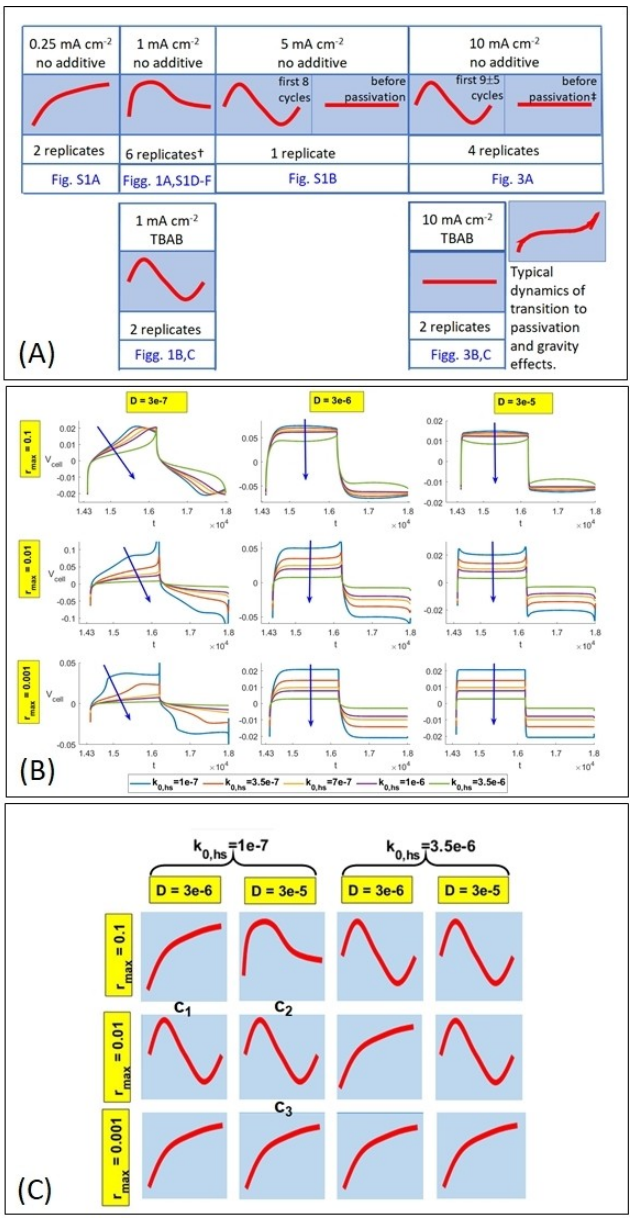

Figure 4. (A) Classification of chronopotentiometric transient types observed during the galvanostatic half-periods. The sketches express the modulus of the overvoltage. †No impact of electrolyte volume changes by a factor of 1.5 (2 replicates) Figure S1-D, no impact of decreasing the depth of discharge by a factor of 5 (1 replicate) Figure S1-E, no impact of using a free electrolyte Figure S1–F. ‡In 2 cases, 3–4 cycles before transition to passivation the initial dynamics was resumed. (B) A representative selection of simulations showing the main chronopotentiometric transient types expressed by the mathematical model. (C) Schematic representation of the parameter space regions in which the experimentally observed chronopotentiometric transient types prevail.

continuous overvoltage growth, (ii) to the formation of a maximum, followed by a relaxation to a voltage asymptote and finally (iii) to a maximum followed by a minimum. In Figure 4-B, we show a representative selection of numerical simulations showing the main chronopotentiometric transient types expressed by the mathematical model, as described in the Supporting Information. In brief, $k_{o,hs}$ is directly proportional to the current density at the metal tips; and r_{max} anticorrelates with the number density of nuclei N_{nucl}. Figure 4-C reports a schematic representation of the parameter space regions in which the experimentally observed chronopotentiometric transient types prevail.

The experimental dynamic shape changes of Panel (A) can thus be followed with the scheme of Panel (C): an initial, increase in D without appreciable change in N_{nucl} ($C_1 \rightarrow C_2$), followed ($C_2 \rightarrow C_3$) by an increase in N_{nucl}. At lower current densities, the same shape is observed until passivation, while at higher ones a transition is noticed to a flat overvoltage, denoting the formation of transient short-circuits. Addition of TBAB brought forward the high-current density scenario, dominated by N_{nucl} increase, already at 1 mA cm^{-2}, and – at 10 mA cm^{-2} – it stabilizes the flat overvoltage behaviour before passivation. Transition to passivation and gravitational effects at the bottom electrode, leading to favoured passivation (for details, see Section S3 of the Supporting Information), are characterized by a monotonic, concave overvoltage growth.

From the data of Table 1, a notable effect of TBAB can be noticed, in slowing down the outgrowth rate. In the absence of additive, outgrowth is faster for higher current densities, but this tendency is reversed by adding TBAB. It is worth noting that, generally, outgrowth starts immediately in the first cycle, and then it tends to level off, but in the experiments carried out at 1 mA cm^{-2} in the presence of TBAB, outgrowth is delayed by 8230 ± 1920 s. Finally, the impact of free vs. immobilized electrolyte seems vanishing.

The data reported in Table 2 show that TBAB additions bring about an extremely high increase in passivation time at 1 mA cm^{-2}, while the effect is reversed at 10 mA cm^{-2}. In fact, in the latter case, the passivation time with TBAB is smaller than in its absence. Moreover, in the additive-free case, increasing the current density brings about a systematic increase in passivation time. Finally, we found a vanishing impact of the following operating conditions: (i) variation of the depth of discharge by a factor of 5; (ii) change of the electrolyte volume by a factor of 1.5; (iii) use of free vs. confined electrolyte. This parametric scenario can be straightforwardly reconciled with well-established electrocrystallization theories.[34] In fact, the positive correlation of current density and number density of nuclei $N_{nucl} \sim r_{max}{}^{-1}$ in the absence of TBAB, and an almost constant and high value of N_{nucl} in the presence of the additive, match with the cathodic surface coverage with adsorbates: electroactive Zn-containing in the former case and principally TBAB in the latter. Moreover, the positive and negative correlations of current density and F_C without and with added TBAB, respectively, show that, in the former case, growth prevails over nucleation, while reductive additive adsorption dominates in the latter chemistry. The tendency to favour growth over nucleation in the absence of TBAB is also in keeping with the increase of the effective diffusion coefficient (increase of spherical vs. planar diffusion) in the low-current density range. Finally, the negative and positive correlations of k_{pass} in the absence and in the presence of TBAB, respectively, are coherent, in the former case, with favoured detachment of the passivating film at higher current densities and, in the latter one, with anodic protection by adsorbed TBAB. The dependence of r_{max}, F_C and k_{pass} on adsorption, points out that this process is key to shape change control. This is coherent with the theoretical framework of the DIB model[32,35] of electrochemical phase formation.

Conclusion

The morphochemical and structural stability of metallic anodes during charge and discharge is of fundamental importance for the development of next-generation rechargeable batteries of both Li and post-Li technologies. Symmetric cell cycling is a simple, but crucial tool to bridge the gap between fundamental electrochemical material-science studies and concrete devices. Often, the reliability of obtained data, their exploitation to gain insight in electrode performance and the understating of the evolution of the materials inside the cell are wanting. This paper proposes an approach to face this issue, applied to the specific case of galvanostatic cycling of Zn symmetrical 2032-type coin-cells with alkaline electrolyte without and with added TBAB. Current densities of 1 and 10 mA cm^{-2} were employed, representing real operating conditions. TBAB is regarded as an additive promoting stable cathodic growth, but so far, in the literature, this conclusion had been drawn from an of incomplete information base, that cannot be safely generalized.

In this study, special emphasis is placed on a multi-method approach, combining electrochemical experiments and 3D X-ray imaging of intact cells, with mathematical modelling. In all investigated conditions, cell cycling is terminated by Zn passivation, but the time to failure, the evolution of the potential profile and the rearrangement of material at the electrodes as well as in the electrolyte are deeply affected by operating parameters. Specifically, at 1 mA cm^{-2} TBAB addition results in a notable (over a factor of 40) increase in time to passivation. In the absence of TBAB, tomography discloses the formation of a thick layer of loose Zn-containing particles at the electrode-electrolyte interface, while presence of the additive brings about strong smoothing. Operation at 10 mA cm^{-2} without additive, does not lead to Zn shape changes that limit cell lifetime, but rather results in longer cycling lifetime (ca. a factor of 3). This results from lower propensity to passivation, causing limited precipitation of Zn compounds in the bulk, as revealed by tomography. Instead TBAB addition at 10 mA cm^{-2} moves up passivation, halving the cell lifetime: this process is correlated with extensive precipitation in the bulk. These results disclose that subtle interactions of TBAB with the Zn surface the Zn oxidation products – at the surface and in the bulk –, result in a strong dependence of the effectiveness of the additive on operating conditions. Thus, additive behaviour cannot be

straightforwardly generalized to conditions not explicitly tested. The described processes can be rationalized in terms of the proposed mathematical model. Parametric analysis shows that the chronopotentiometric transients resulting from galvanostatic cycling are chiefly controlled by the nuclei number density, that correlates with the cathode surface occupation by adsorbates: either Zn-containing intermediates or TBAB. In addition, surface coverage with adsorbates drives the metal outgrowth rate in the cathodic period and the passivation rate in the anodic one.

The complementary electrochemical, modelling and imaging approach proposed in this paper, paves the way to a deeper understanding of the performance of metal anodes and provides a tool for the knowledge-based development of materials modifications, in view of better cyclability with different electrolytes and operating conditions.

Experimental Section

Electrochemical methods

Symmetrical Zn/Zn cells with alkaline electrolyte were assembled with an EL-CELL electrochemical split cell, in which the electrodes are mounted in the horizontal position. The electrodes consisted of two as-rolled Zn discs (99.98% Alfa Aesar, 0.25 mm thick and 18 mm diameter) that were degreased with acetone, rinsed with milli-Q water and put in contact with two austenitic stainless steel (AISI 304) current collectors (0.6 mm thick, 18 mm diameter). The experiments were performed in two different electrolyte configurations: with a separator soaked with a calibrated amount of electrolyte, or with a free electrolyte. Specifically, we employed 0.42 mm thick glass fibre separators EL-CELL ECC1-01-0012-E, soaked in 200 µl of electrolyte (other cases were also considered, to test the sensitivity of cycling results to these experimental parameters: more details are provided in the Supporting Information). In the free-electrolyte experiments, the electrodes were kept separated by an O-ring (2.50 mm thick, 18 mm outer diameter) and the cell was filled with 400 µl of electrolyte. The alkaline electrolyte consisted of 6 M KOH + 0.1 M ZnO, without or with addition of 0.3 mM tetrabutylammonium bromide (TBAB, Fluka). GCD cycles were performed at 1 and 10 mA cm^{-2} with 60 min periods (30 min positive and 30 min negative current). To gain more insight into the sensitivity of cell cycling performance, we also carried out tests in a selection of different operating conditions, as described in the Supporting Information. Cycling was performed with a Versastat3F potentiostat/galvanostat. The potential time-series resulting from cycling have been analysed with the model, the key mathematical features of which are summarized in Section S3 of the Supporting Information.

Characterisation by X-ray computed tomography (µ-CT)

X-ray µ-CT is a non-destructive technique based on the 3D mapping of the X-ray attenuation coefficient across the investigated sample.[36–39] Through virtual slicing of the reconstructed sample volume and applying image processing and analysis 3D tools, it is possible to achieve a morpho-textural characterization of the internal features present in the sample. This technique was applied in this study, using both a synchrotron-based and a laboratory-based X-ray sources available at the Elettra synchrotron facility in Basovizza (Trieste, Italy).

Microfocus X-ray computed tomography (µ-CT) – Laboratory-based X-ray µ-CT data have been acquired on the whole, centimeter-sized cells (see Section 4.1) at the TomoLab station of Elettra.[40] This is a fully customized instrument based on a sealed microfocus X-ray source (Hamamatsu L9181, Japan), which guarantees a minimum focal spot size of 5 µm working in cone-beam geometry. With this set up it is possible to achieve a maximum spatial resolution close to the focal spot size of the source and to operate in absorption and propagation-based phase-contrast mode.[37–39] More details regarding the TomoLab station and the X-ray µ-CT data analysis protocol are provided in Section S5.1 of the Supporting Information. The TomoLab instrument has previously been successfully used to obtain 3D images of cells with Zn sponge anodes and valuable information about phase morphology and volume distribution.[41]

Phase-contrast synchrotron radiation computed microtomography (SR µ-CT) – SR µ-CT data were acquired at the SYRMEP beamline of Elettra.[42] At SYRMEP, a bending magnet source located at about 23 m from the sample delivers a nearly parallel X-ray beam characterized by a high spatial coherence. These characteristics allow the use propagation-based phase-contrast imaging enhancing the visibility of interfaces related to abrupt phase changes in the investigated samples. In comparison to absorption mode, phase images look sharper (in edge-detection mode[43]), and objects smaller than the pixel size of the detector or with close refraction index could be detected and analyzed.[37–39] In this work, phase-contrast SR µ-CT was used to characterize in 3D the matrix morphology of a sub-volume an entire cell at higher spatial and contrast resolution with respect to laboratory µ-CT images. More instrumental details concerning the experimental set up used at SYRMEP and the SR µ-CT data analysis methods are given in Section S5.2 of the Supporting Information.

Scanning electron microscopy

Ex-situ morphological studies of the electrodes cycled in the free electrolyte setup were carried out with an EVO 40 (Zeiss) Scanning Electrode Microscope (SEM).

Acknowledgements

Open Access Funding provided by Politecnico di Milano within the CRUI-CARE Agreement.

Conflict of Interest

The authors declare no conflict of interest.

Data Availability Statement

Research data are not shared.

Keywords: Cycling · Dendrite · Mathematical modelling · Passivation · Zinc

[1] V. Mathew, B. Sambandam, S. Kim, S. Kim, S. Park, S. Lee, M. H. Alfaruqi, V. S. Islam, D. Y. Putro, J.-Y. Hwang, Y. Sun, J. Kim, *ACS Energy Lett.* **2020**, *5*, 2376–2400.
[2] Y. Shi, Y. Chen, L. Shi, K. Wang, B. Wang, L. Li, Y. Ma, Y. Li, Z. Sun, W. Ali, S. Ding, *Small* **2020**, *16*, 1–28.
[3] Y. Zhang, Z. Chen, H. Qiu, W. Yang, Z. Zhao, J. Zhao, G. Cui, *NPG Asia Mater.* **2020**, *12*, 1–24.
[4] D. Yang, H. Tan, X. Rui, Y. Yu, *Electrochem. Energy Rev.* **2019**, *2*, 395–427.
[5] T. S. Lee, *J. Electrochem. Soc.* **1971**, *118*, 1278–1282.
[6] Y. Sawada, *Phys. A* **1986**, *140*, 134–141.
[7] A. R. Despic, J. Diggle, J. O'M. Bockris, *J. Electrochem. Soc.* **1968**, *5*, 507–508.
[8] C. Cachet, U. Ströder, R. Wiart, *Electrochim. Acta* **1982**, *27*, 903–908.
[9] Z. Zhao, X. Fan, J. Ding, W. Hu, C. Zhong, J. Lu, *ACS Energy Lett.* **2019**, *4*, 2259–2270.
[10] D. P. Trudgeon, K. Qiu, X. Li, T. Mallick, O. O. Taiwo, B. Chakrabarti, V. Yufit, N. P. Brandon, D. Crevillen-Garcia, A. Shah, *J. Power Sources* **2019**, *412*, 44–54.
[11] W. Lu, C. Xie, H. Zhang, X. Li, *ChemSusChem.* **2018**, *11*, 1–12.
[12] B. Bozzini, F. Rossi, C. Mele, M. Boniardi, *ChemElectroChem* **2020**, *7*, 1752–1764.
[13] J. M. Wang, L. Zhang, C. Zhang, J. Q. Zhang, *J. Power Sources* **2001**, *102*, 139–143.
[14] Y. H. Wen, T. Wang, J. Cheng, J. Q. Pan, G. P. Cao, Y. S. Yang, *Electrochim. Acta* **2012**, *59*, 64–68.
[15] Y. H. Wen, T. Wang, J. Cheng, J. Q. Pan, G. P. Cao, Y. S. Yang, *Adv. Mater. Res.* **2012**, *396*, 18–23.
[16] C. Xu, B. Li, H. Du, F. Kang, *Angew. Chem. Int. Ed.* **2012**, *51*, 933–935; *Angew. Chem.* **2012**, *124*, 957–959.
[17] K. Hu, X. Guan, R. Lv, G. Li, Z. Hu, L. Ren, A. Wang, X. Liu, J. Luo, *Chem. Eng. J.* **2020**, *396*, 125363 (7 pages).
[18] M. Shimizu, K. Hirahara, S. Arai, *Phys. Chem. Chem. Phys.* **2019**, *21*, 7045–7052.
[19] H. Pan, Y. Shao, P. Yan, Y. Cheng, K. S. Han, Z. Nie, C. Wang, J. Yang, X. Li, P. Bhattacharya, K. T. Mueller, J. Liu, *Nat. Energy* **2016**, *1*, 1–7.
[20] W. Yu, W. Shang, X. Xiao, P. Tan, B. Chen, Z. Wu, H. Xu, M. Ni, *J. Power Sources* **2020**, *453*, 227856 (8 pages).
[21] H. Glatz, E. Tervoort, D. Kundu, *ACS Appl. Mater. Interfaces* **2020**, *12*, 3522–3530.
[22] S. Wang, K. Q. Zhang, Q. Y. Xu, M. Wang, R. W. Peng, Z. Zhang, N.-B. Ming, *J. Phys. Soc. Jpn.* **2003**, *72*, 1574–1580.
[23] R. Nishikiori, S. Morimoto, Y. Fujiwara, Y. Tanimoto, *Appl. Magn. Reson.* **2011**, *41*, 221–227.
[24] A. N. Chen, F. H. Cao, W. J. Liu, L. Y. Zheng, Z. Zhang, J. Q. Zhang, C. N. Cao, *Trans. Nonferrous Met. Soc. China* **2012**, *22*, 228–240.
[25] I. Mogi, H. Kikuya, K. Watanabe, S. Awaji, M. Motokawa, *Chem. Lett.* **1996**, *25*, 673–674.
[26] R. C. V. Piatti, J. J. Podestá, A. J. Arvía, *Electrochim. Acta* **1980**, *25*, 827–831.
[27] B. Bozzini, C. Mele, M. C. D'Autilia, I. Sgura, *Metall. Ital.* **2019**, *7–8*, 33–30.
[28] A. R. Despić, D. Jovanović, T. Rakić, *Electrochim. Acta* **1976**, *21*, 63–77.
[29] L. M. Baugh, A. R. Baikie, *Electrochim. Acta* **1985**, *30*, 1173–1183.
[30] M. N. Hull, J. E. Ellison, J. E. Toni, *J. Electrochem. Soc.* **1970**, 117, 192–198.
[31] K. Krischer, H. Varela, *Oscillations and Other Dynamic Instabilities. In Handbook of Fuel Cells*, **2010**, https://doi.org/10.1002/9780470974001.f206052.
[32] B. Bozzini, M. C. D'Autilia, C. Mele, I. Sgura, *Appl. Eng. Sci.* **2021**, *5*, 100033 (13 pages).
[33] C. Mele, A. Bilotta, P. Bocchetta, B. Bozzini, *J. Appl. Electrochem.* **2017**, *47*, 877–888.
[34] B. Bozzini, D. Lacitignola, C. Mele, I. Sgura, *Note di Mat.* **2012**, *21*, 7–46.
[35] D. Lacitignola, B. Bozzini, M. Frittelli, I. Sgura, *Commun. Nonlinear Sci. Numer. Simul.* **2017**, *48*, 484–508.
[36] J. Baruchel, J. Y. Buffière, E. Maire, P. Merle, G. Peix, *Hermes Sci. Publ.* **2000**, *31*, 1–209.
[37] E. Maire, P. J. Withers, *Int. Mater. Rev.* **2014**, *59*, 1–43.
[38] S. C. Mayo, A. W. Stevenson, S. W. Wilkins, *Materials* **2012**, *5*, 937–965.
[39] D. Zandomeneghi, M. Voltolini, L. Mancini, F. Brun, D. Dreossi, M. Polacci, *Geosphere* **2010**, *6*, 793–804.
[40] Tomolab Website: https://www.elettra.trieste.it/lightsources/labs-and-services/tomolab/tomolab.html.
[41] B. Bozzini, C. Mele, A. Veneziano, N. Sodini, G. Lanzafame, A. Taurino, L. Mancini, *ACS Appl. Mater. Interfaces* **2020**, *3*, 4931–4940.
[42] G. Tromba, R. Longo, A. Abrami, F. Arfelli, A. Astolfo, P. Bregant, F. Brun, K. Casarin, V. Chenda, D. Dreossi, M. Hola, J. Kaiser, L. Mancini, R. H. Menk, E. Quai, E. Quaia, L. Rigon, T. Rokvic, N. Sodini, D. Sanabor, E. Schultke, M. Tonutti, A. Vascotto, F. Zanconati, M. Cova, E. Castelli, *AIP Conf. Proc.* **2010**, *1266*, 18–23.
[43] P. Cloetens, M. Pateyron-Salomé, J. Y. Buffière, G. Peix, J. Baruchel, F. Peyrin, M. Schlenker, *J. Appl. Phys.* **1997**, *81*, 5878–5886.

Manuscript received: November 14, 2021
Revised manuscript received: December 28, 2021
Accepted manuscript online: January 4, 2022